

Spin Hall photoconductance in a 3D topological insulator at room temperature

Paul Seifert¹, Kristina Vaklinova², Sergey Ganichev³, Klaus Kern^{2,4}, Marko Burghard² and Alexander W. Holleitner^{1,*}

¹Walter Schottky Institut and Physik-Department, Technische Universität München, Am Coulombwall 4a, D-85748 Garching, Germany.

²Max-Planck-Institut für Festkörperforschung, Heisenbergstraße 1, D-70569 Stuttgart, Germany.

³Terahertz Center, University of Regensburg, D-93040 Regensburg, Germany.

⁴Institut de Physique, Ecole Polytechnique Fédérale de Lausanne, CH-1015 Lausanne, Switzerland.

Three-dimensional topological insulators are a class of Dirac materials, wherein strong spin-orbit coupling leads to two-dimensional surface states. The latter feature spin-momentum locking, i.e., each momentum vector is associated with a spin locked perpendicularly to it in the surface plane. While the principal spin generation capability of topological insulators is well established, comparatively little is known about the interaction of the spins with external stimuli like polarized light. We observe a helical, bias-dependent photoconductance at the lateral edges of topological $\text{Bi}_2\text{Te}_2\text{Se}$ platelets for perpendicular incidence of light. The same edges exhibit also a finite bias-dependent Kerr angle, indicative of spin accumulation induced by a transversal spin Hall effect in the bulk states of the $\text{Bi}_2\text{Te}_2\text{Se}$ platelets. A symmetry analysis shows that the helical photoconductance is distinct to common longitudinal photoconductance and photocurrent phenomena, but consistent with the accumulated spins being transported in the side facets of the platelets. Our findings demonstrate that spin effects in the facets of 3D topological insulators can be addressed and read-out in optoelectronic devices even at room temperatures.

Selectively addressing the 2D surface states (SSs) of 3D topological insulators (TIs)¹⁻⁴ in electrical transport experiments is challenging due to the intrinsic doping of TIs, resulting in sizable contribution of the bulk states (BSs) to the conductivity. Nevertheless, electrically induced spin-polarized currents due to spin-momentum locking⁵ have been demonstrated in lateral spin valve devices with a ferromagnetic spin detector based on a number of bismuth and antimony chalcogenides⁶⁻⁹. Alternatively, the SSs and their dynamics can be probed via optical excitation of photocurrents, whose decay enables access to the spin-relaxation time of both SSs and BSs in 3D TIs¹⁰⁻¹⁵. Time-resolved ARPES experiments have demonstrated dynamics control of spin-polarized currents in Sb₂Te₃^{16,17} and Bi₂Se₃^{11,18}, as well as emergent Floquet-Bloch states due to hybridization of the SSs and pulsed circularly polarized light (CPL)¹⁹. According to theory^{20,21}, CPL can couple to the electron spin in a material and the helicity of the incident photons determines the spin-polarization of the resultant in-plane photocurrents due to asymmetric excitation of spin-up and spin-down carriers. This circular photogalvanic effect has been experimentally demonstrated in Bi₂Se₃²²⁻²⁴, Sb₂Te₃²⁵, and (Bi_{1-x}Sb_x)₂Te₃²⁶ and can be tuned via electrostatic gating²³, Fermi energy tuning²⁶, and proximity interactions²⁷. In addition, a helicity-dependent photovoltaic effect has been reported for normally incident light in vicinity of the metal contacts on a Bi₂Se₃ nanosheet²⁸.

Importantly, along with the SS-generated in-plane spin polarization, the strong spin-orbit coupling (SOC) of the bulk bands can give rise to out-of-plane spin polarization diffusing perpendicularly to the applied current direction via the intrinsic spin Hall effect²⁹⁻³³. Theory further predicts that a bulk-mediated diffusion of spin density can take place between the top and bottom TI surfaces²⁹. So far, only little experimental data are available on bulk spin currents in 3D TIs. Spin-charge conversion via the inverse spin Hall effect has been demonstrated for a TI/metallic ferromagnet heterostructure³⁴. In general, however, SO-enhanced scattering suggests strongly reduced spin diffusion lengths in 3D TIs, which makes spin detection and manipulation challenging. In the present work, we explore the spin texture of Bi₂Te₂Se (BTS) platelets under electrical current flow using two complementary experimental methods, namely helical photoconductance measurements and magneto-optical Kerr microscopy. Our data is fully consistent with a bulk-spin Hall effect generating a spin accumulation in the side-facets of the BTS platelets, which can be read-out as a helical photoconductance with a lifetime characteristic of the SSs in the platelets' side-facets.

We contact individual BTS platelets on a transparent sapphire substrate by two Ti/Au contacts, and focus a circularly polarized laser with a photon energy of 1.54 eV normally incident onto the platelets (Fig. 1a and Methods). We apply a bias voltage V_{sd} between the contacts, such that a local electron current density j flows in the sample (black arrow in Fig. 1a). Figure 1b presents an optical microscope image of an exemplary device, comprising a BTS platelet with a width of 8.9 μm and a height of 90 nm, while the Au-contacts have a distance of 10 μm . We record the optical transmission signal of the platelet upon scanning the laser with a spot size of $\sim 1.5 \mu\text{m}$ across (Fig. 1c) and define three positions, specifically the left edge (blue circle), the center (gray circle), and the right edge (red circle). The corresponding photoconductance map acquired under an applied bias voltage V_{sd} of 1.2 V (Fig. 1d) displays a helicity dependent photoconductance with opposite sign at both edges. In particular, these signals reflect the difference $\Delta G_{\text{helical}} = G_{\text{helical}}(\sigma^+) - G_{\text{helical}}(\sigma^-)$ of the photoconductance G_{helical} , which depends on the circularly right (σ^+) and right (σ^-) polarized light. The absence of a photoconductance signal

away from the edges is consistent with the in-plane spin polarization associated to the SSs at the top/bottom surface of the platelet and the normal incidence of the circularly polarized light¹⁷. In order to gain further insight into the origin of the edge signals, we use a quarter wave plate to resolve the sign change of G_{helical} as a function of helicity (Figs. 1e to g, and Supplementary Fig. 1). In the following, we interpret G_{helical} to occur in the topological side surfaces of the BTS platelets as a consequence of spin-accumulation caused by the bulk spin-Hall effect²⁹⁻³³. In this scenario, the spin accumulation induced by the bias-driven current density \mathbf{j} (black arrow in Fig. 1a) is characterized by an out-of-plane spin polarization pointing in opposite directions at the left and right edge of the BTS platelet (blue and red arrows).

Fig. 2a reveals that $\Delta G_{\text{helical}}$ depends linearly on the laser power P_{laser} (up to 12 mW), without reaching saturation. By contrast, the polarization-independent photoconductance G_{photo} displays a polarity change vs. laser power, as discussed in detail in [12]. Correspondingly, we attribute the polarity change to a saturation of the lifetime-limited photoconductance in the bulk states and the one in the SSs at the top and bottom surface for $P_{\text{laser}} \geq 5$ mW, while a bolometric photoconductance with a negative sign dominates the high power regime. We note that a bolometric photoconductance is driven by a heated phonon bath of the BTS platelets¹². Fig. 2a highlights that $\Delta G_{\text{helical}}$ captures an effect that is clearly distinguished from the conventional longitudinal photoconductance effects in the bulk and surface states of BTS. This difference becomes particularly evident at a laser power of ~ 6 mW, where the polarization-independent G_{photo} is zero, while $\Delta G_{\text{helical}}$ can be fully controlled with the laser polarization. The latter observation indicates that $\Delta G_{\text{helical}}$ is not a modulation of G_{photo} . To a first approximation, $\Delta G_{\text{helical}}$ is decoupled from the helicity independent longitudinal photoconductance, which justifies our approach of subtracting the helicity independent conductance contributions as an offset and only evaluating the helicity dependent photoconductance (cf. Supplementary Fig. 1).

The schematic sketches of the excitation configuration of our photoconductance experiment in Figs. 3a and b define the electron and photon wave vectors k_{electron} and k_{photon} , as well as the spin polarization \mathbf{S} at the left and right edges of the BTS platelet. As apparent from Figs. 3c to h, a finite G_{helical} is observed only at a finite bias voltage, thereby excluding G_{helical} as a photocurrent effect which would have a finite magnitude at zero bias. We note that for $V_{\text{sd}} = 0$ (Figs. 3d and g), the originally detected signal $I_{\text{helical}} \sim 0$ nA is plotted instead of G_{helical} , as an experimental conductance is not defined at zero bias. As another relevant observation, G_{helical} flips by π when either the bias V_{sd} is reversed (cf. Fig. 3c vs. e and Fig. 3f vs. h), or when the laser spot position is exchanged between the left and right platelet edge.

Table 1 summarizes the experimentally observed symmetry characteristics of G_{helical} as concluded from Figs. 1-3, and contrast them with those of the polarization-independent G_{photo} and of helical photocurrents in materials with a broken symmetry^{35,36}. The latter type of current is denoted as ' I_{edge} ' in the table, in order to associate it with the circular photogalvanic effect which is well documented for topological insulators^{20-24,36}. From the observed bias dependence, any photocurrent effect can be excluded as origin of G_{helical} . However, it should be emphasized that such currents indeed emerge at the side-facets of the BTS platelets, although their amplitude is very small (cf. Supplementary Fig. S2). The small amplitude is explainable by the fact that the optical cross section of the side facets is about 100 times smaller compared to that of the bulk volume in the BTS platelets. It is furthermore noteworthy that the helical photoconductance G_{helical} does not depend on the direction of the photon wavevector k_{photon} (cf. Fig. 3 vs. Supplementary

Figs. 3 and 4). Moreover, from the polarity change of G_{helical} with V_{sd} , one can exclude a longitudinal photoconductance response based upon the following argument. In case of a longitudinal response, the sign of G_{helical} would reflect the preferred current direction in x-direction upon laser illumination. From a symmetry perspective, a current reversal is equivalent to a simultaneous operation ‘left edge’ to ‘right edge’ and a rotation of the sample by a spatial angle of π . The latter combined operations have to be an even operation due to rotational symmetry, while a bias reversal of G_{helical} is odd (cf. table 1), which contradicts the experimental findings. Nonetheless, there remains a process which is fully consistent with the observed symmetries, specifically a transverse photoconductance. In fact, the latter can effectively modulate the conductivity along the edges of the BTS platelets, and thus supports the assumption of a bulk spin current in 3D TIs, which has been analytically predicted based upon topological arguments. Recently, bulk spin currents have been indentified as a possible spin generation mechanism in 3D topological insulators via the spin Hall effect²⁹⁻³³. Indeed, this mechanism would yield an accumulated spin polarization parallel to the SS-based spin polarization in the side facets of BTS platelets (cf. red and blue arrows in Fig. 1a), as recently verified and discussed^{29-33,37}. Furthermore, it should result in an opposite spin accumulation at the opposite edges of the BTS platelets, and also reverse sign upon reversing the longitudinal charge current direction.

In order to verify the presence of vertically aligned spins accumulated at the edges of the BTS platelets, we investigate the device by magneto-optical Kerr-microscopy. The detected Kerr angles θ_k (Figs. 4a - c) are bias-dependent and their sign is opposite at the opposite edges of the platelet. Likewise, the sign of θ_k at the edges switches with the sign of the applied bias (Figs. 4a and c), whereas θ_k vanishes at the center of the platelet (Fig. 4b). In close correspondence, also G_{helical} follows such bias and position dependence (Figs. 4d to f).

The above outlined mechanism of helicity dependent photoconductance in BTS can be rationalized by a microscopic model as follows. The spin relaxation of photogenerated charge and spin carriers in 3D TIs, including BTS, occurs on ultrafast timescales on the order of 100 fs¹¹. This fast relaxation suggests that the underlying spin dynamics of G_{helical} is governed by spin diffusion rather than a spin precession process³⁰. The spin diffusion length in Bi_2Se_3 was experimentally determined to be below 10 nm at room temperature³⁸. This length is significantly smaller than both, the diffusion length of hot carriers that ranges between 200 and 300 nm in bismuth-chalcogenides³⁹, and the laser spot size of $\sim 1.5 \mu\text{m}$ in our experiment. Moreover, we observe that G_{helical} is located at the edges of the BTS platelets (Fig. 1d). Interestingly, we can observe the edge-localized G_{helical} also in a BTS platelet with a spatial width as small as $d_{\text{platelet}} \sim 300 \text{ nm}$ (cf. Supplementary Fig. 5). The latter observation is consistent with a dominating spin diffusion length smaller than $\frac{1}{2} \cdot d_{\text{platelet}} \sim 150 \text{ nm}$ at the edges. It has been reported that the inverse Spin Hall effect in the bulk states of n -doped Bi_2Se_3 is comparable to or even dominating over the surface Edelstein effects^{37, 38}. Hence, a bulk spin Hall effect should be favorable over an out-of-plan spin component due to warping effects in the top and bottom surface of the BTS platelets²⁰. Moreover, the side facets are expected to exhibit a spin-momentum locking⁴⁰ even in the presence of disorder. Under sufficiently high surface disorder, the spin relaxation time has been predicted to be increased similar as the D’yakonov–Perel mechanism in a motional narrowing regime²⁹. Analogously, the spin generation efficiency and surface conductivity are suggested to be strongly enhanced at the disordered facets of the BTS platelets²⁹, as previously demonstrated for surfaces of $\text{Bi}_1\text{Sb}_1\text{TeSe}_2$ ⁴¹. Along these lines, we interpret G_{helical} as a measure

of optically excited spins which are driven by the spin Hall effect to (or away from) the edges (blue and red arrows in Fig. 1a), where they experience an increased (or decreased) conductivity. This scenario is able to account for all our experimental findings. In particular, it explains not only the polarization dependence in Figs. 1e to g, but also all other experimental observations summarized in table 1. This interpretation suggests that G_{helical} is a read-out of a bulk spin accumulation by scattering into the surface states of the side-facets in the BTS platelets²⁹. Importantly, we determine the decay time of G_{helical} to be $\tau_{\text{decay}} = (463 \pm 13)$ ps (cf. Supplementary Fig. 6). This value, while exceeding the spin relaxation time by far, agrees very well with the surface lifetime of the BTS platelets^{12,42}; thereby strongly supporting the above mechanism. In other words, after a pulsed laser excitation, G_{helical} prevails as long as τ_{decay} within the surface states of the side facets.

Overall, the possibility to optically detect the spin Hall effect-driven spins at structurally disordered 3D TI surfaces relaxes the technical demands on device fabrications, thus underscoring the theoretical prediction that surface disorder in 3D TIs might even be beneficial for spintronic applications²⁹. Furthermore, the demonstrated read-out principle might prove useful also for probing the spatial accumulation of spins in related materials such as Weyl semimetals.

Methods

Bi₂Te₂Se platelet growth and charge carrier density. BTS platelets are grown by a catalyst-free vapor-solid method on Si substrates covered by a 300 nm thick SiO₂ layer. Bi₂Se₃ and Bi₂Te₃ crystal sources (99.999% purity) are heated up to ~580°C in a tube furnace. Ultrapure argon gas transports the evaporated material to the growth substrates, which are heated to 450°-480°C during a growth time of 30 min. The pressure in the furnace is maintained at 75-85 mbar at Argon flow rate of 150 sccm. Thus obtained platelets have a length in the range of 5-60 μm, a lateral width of 0.05-1 μm, and a thickness of 15-200 nm. The platelets are mechanically transferred onto Al₂O₃ substrates and lithographically contacted by metal strips made of thermally evaporated Ti/Au (10 nm/250 nm). Four-terminal Hall-measurements on single BTS platelets with a width of a few hundreds of nm revealed n-doping character, with an electron concentration of 10¹⁹ cm⁻³ at room temperature.

Time-integrated photoconductance spectroscopy. For the excitation of the BTS platelets, we use a Ti-sapphire laser that emits either light at laser pulses with 150 fs pulse duration and a repetition rate of 76 MHz. In all cases, the photon energy is set to be 1.54 eV. The position of the laser spot with size ~1.5 μm is set with a spatial resolution of ~100 nm. The helical photoconductance is measured with a standard lock-in measurement technique, where the laser is modulated by a chopper at a frequency of $f_{\text{chop}} = 2.7$ kHz or a piezoelectric modulator (PEM) at a frequency of 50 kHz. The PEM is set to switch the polarization of the exciting laser between σ^- and σ^+ polarized light. Alternatively, we utilize a quarter wave plate to control the circular polarization of the laser. All presented experiments are performed at room temperature and in a vacuum chamber at $\sim 5 \times 10^{-6}$ mbar.

Autocorrelation photoconductance spectroscopy. For characterizing the decay dynamics of G_{helical} , we split the pulsed laser beam into a pump and a probe pulse with comparable intensity, and focus the pump- (probe-) from the front (back) onto the BTS platelets (cf. Supplementary Fig. S4). The probe-beam, which is chopped at a frequency of ~1930 Hz, hits the sample at a time delay Δt . The time-resolved autocorrelation signal is then detected with a lock-in amplifier on the sum-frequency of the pump- and the probe-pulse as a function of the time delay Δt . The probe-pulse is delayed via a mechanical delay stage.

Magneto-optical Kerr microscopy. For the Kerr-effect spectroscopy we utilize the same measurement setup as for the photoconductance spectroscopy. The laser is polarized purely linearly. The polarization of the reflected light is rotated by 45° via a half-waveplate. Afterwards, a Wollaston prism splits the reflected light into two cross-polarized beams with an angle of 20° which are detected by two balanced photodetectors. The difference- and sum-signal of the detectors are detected by two lock-in amplifiers at a frequency of 2.7 kHz. To calibrate the reflected signal, the laser-spot is positioned onto a normally reflecting surface (e.g. gold) and the half-waveplate is adjusted, such that the difference signal of the detectors is perfectly zero. Any rotation of the reflected light's polarization shifts the balance between the detectors, which is then detected in the difference- but not in the sum-signal. Hence the sum-signal is used to calibrate the difference-signal in order to get rid of laser-intensity based noise and fluctuations.

Acknowledgements

We acknowledge S. Tarasenko, H. Hübl, and M. Münzenberg for very helpful discussions, and the DFG (Projects HO 3324/8-2 and SFB 1277-A04) as well as the ERC-grant NanoREAL for financial support.

Author contributions

P.S. and A.W.H. designed the experiments, K.V., M.B., K.K. provided the materials, P.S. performed all experiments, and P.S., A.W.H., S.G., K.V., K.K., M.B. analyzed the data and wrote the manuscript.

Additional information

Supporting information is available online.

Competing financial interests

The authors declare no competing interests.

References

1. Hasan, M. Z. and Kane, C. L. *Colloquium: Topological Insulators Rev. Mod. Phys.* **82**, 3045 (2010).
2. Ando, Y. Topological Insulator Materials. *J. Phys. Soc. Japan* **82**, 102001 (2013).
3. Wehling, T. O., Black-Schaffer, A. M. and Balatsky, A. V. Dirac materials. *Adv. Phys.* **63**, 1(2014).
4. Xia, Y. *et al.* Observation of a large-gap topological-insulator class with a single Dirac cone on the surface. *Nat. Phys.* **5**, 398 (2009).
5. Hsieh, D. *et al.* Observation of unconventional quantum spin textures in topological insulators. *Science* **323**, 919 (2009).
6. H., L. *et al.* Electrical detection of charge-current-induced spin polarization due to spin-momentum locking in Bi_2Se_3 . *Nat. Nano* **9**, 218 (2014).
7. Tang, J. *et al.* Electrical detection of spin-polarized surface states conduction in $(\text{Bi}_{0.53}\text{Sb}_{0.47})_2\text{Te}_3$ topological insulator. *Nano Lett.* **14**, 5423 (2014).
8. Ando, Y. *et al.* Electrical detection of the spin polarization due to charge flow in the surface state of the topological insulator $\text{Bi}_{1.5}\text{Sb}_{0.5}\text{Te}_{1.7}\text{Se}_{1.3}$. *Nano Lett.* **14**, 6226 (2014).
9. Tian, J., Miotkowski, I., Hong, S. and Chen, Y. P. Electrical injection and detection of spin-polarized currents in topological insulator $\text{Bi}_2\text{Te}_2\text{Se}$. *Sci. Rep.* **5**, (2015).
10. Neupane, M. *et al.* Topological surface states and Dirac point tuning in ternary topological insulators. *Phys. Rev. B* **85**, 235406 (2012).
11. Sobota, J. A. *et al.* Ultrafast optical excitation of a persistent surface-state population in the topological insulator Bi_2Se_3 . *Phys. Rev. Lett.* **108**, 117403 (2012).
12. Seifert, P., Vaklinova, K., Kern, K., Burghard, M. and Holleitner, A. Surface State-Dominated Photoconduction and THz Generation in Topological $\text{Bi}_2\text{Te}_2\text{Se}$ Nanowires. *Nano Lett.* **17**, 973 (2017).
13. Plank H. *et al.* Opto-Electronic Characterization of Three Dimensional Topological Insulators. *J. Appl. Phys.* **120**, 165301 (2016)
14. Yeats, A. L.; *et al.* Persistent optical gating of a topological insulator. *Sci. Adv.* **1**, 9, e1500640 (2015)
15. Braun, L. *et al.* Ultrafast photocurrents at the surface of the three-dimensional topological insulator Bi_2Se_3 . *Nat. Commun.* **7**, 13259 (2016).
16. Zhu, S. *et al.* Ultrafast electron dynamics at the Dirac node of the topological insulator Sb_2Te_3 . *Sci. Rep.* **5**, 13213 (2015).
17. Sánchez-Barriga, J. *et al.* Ultrafast spin-polarization control of Dirac fermions in topological insulators. *Phys. Rev. B* **93**, 155426 (2016).
18. Wang, Y. H. *et al.* Measurement of intrinsic dirac fermion cooling on the surface of the topological insulator Bi_2Se_3 using time-resolved and angle-resolved photoemission spectroscopy. *Phys. Rev. Lett.* **109**, 127401 (2012).
19. Wang, Y. H., Steinberg, H., Jarillo-Herrero, P. and Gedik, N. Observation of Floquet-Bloch States on the Surface of a Topological Insulator. *Science* **342**, 453 (2013).
20. Hosur, P. Circular photogalvanic effect on topological insulator surfaces: Berry-curvature-dependent response. *Phys. Rev. B* **83**, 35309 (2011).

21. Fregoso, B. M., Wang, Y. H., Gedik, N. and Galitski, V. Driven electronic states at the surface of a topological insulator. *Phys. Rev. B* **88**, 155129 (2013).
22. McIver, J. W. *et al.* Control over topological insulator photocurrents with light polarization. *Nat Nano* **7**, 96 (2012).
23. Duan, J. *et al.* Identification of helicity-dependent photocurrents from topological surface states in Bi₂Se₃ gated by ionic liquid. *Sci. Rep.* **4**, 4889 (2014).
24. Kastl, C., Karnetzky, C., Karl, H. and Holleitner, A. W. Ultrafast helicity control of surface currents in topological insulators with near-unity fidelity. *Nat. Commun.* **6**, 6617 (2015).
25. Kuroda, K., Reimann, J., Gdde, J. and Hfer, U. Generation of transient photocurrents in the topological surface state of Sb₂Te₃ by direct optical excitation with midinfrared pulses. *Phys. Rev. Lett.* **116**, 76801 (2016).
26. Okada, K. N. *et al.* Enhanced photogalvanic current in topological insulators via Fermi energy tuning. *Phys. Rev. B* **93**, 81403 (2016).
27. Semenov, Y. G., Li, X. & Kim, K. W. Tunable photogalvanic effect on topological insulator surfaces via proximity interactions. *Phys. Rev. B* **86**, 201401 (2012).
28. Besbas, J. *et al.* Helicity-dependent photovoltaic effect Bi₂Se₃ under normal incident light. *Adv. Opt. Mater.* **4**, 1642 (2016).
29. Peng, X., Yang, Y., Singh, R. R. P., Savrasov, S. Y. and Yu, D. Spin generation via bulk spin current in three-dimensional topological insulators. *Nat. Commun.* **7**, 10878 (2016).
30. Sinova, J. *et al.* Spin Hall effects. *Rev Mod Phys.* **87**, 1213 (2015).
31. Stern, N.P. *et al.* Current-induced polarization and the spin hall effect at room temperature. *Phys. Rev. Lett.* **97**, 126603 (2006).
32. Sih, V. *et al.* Generating Spin Currents in Semiconductors with the Spin Hall Effect. *Phys. Rev. Lett.* **97**, 096605 (2006).
33. Kato, Y. K. *et al.* Observation of the spin Hall effect in semiconductors. *Science* **306**, 1910 (2004).
34. Dyakonov, M. I. and Perel, V. I. Spin relaxation of conduction electrons in noncentrosymmetric semiconductors. *Sov. Phys. Solid State* **13**, 3023 (1972).
35. S. D. Ganichev and W. Prettl, *J. Phys.: Condens. Matter* **15**, R935 (2003).
36. Dantscher, K. *et al.* Photogalvanic probing of helical edge channels in two-dimensional HgTe topological insulators. *Phys. Rev. B* **95**, 201103 (2017).
37. Jamali, M. *et al.* Giant Spin Pumping and Inverse Spin Hall Effect in the Presence of Surface and Bulk Spin–Orbit Coupling of Topological Insulator Bi₂Se₃. *Nano Lett.* **15**, 7126 (2015).
38. Deorani, P. *et al.* Observation of inverse spin Hall effect in bismuth selenide. *Phys. Rev. B.* **90**, 094403 (2014).
39. Kastl, C. *et al.* Local photocurrent generation in thin films of the topological insulator Bi₂Se₃. *Appl. Phys. Lett.* **101**, 251110 (2012).
40. Villanova, J. W. *et al.* Spin textures of topological surface states at side surfaces of Bi₂Se₃ from first principles *Phys. Rev. B* **93**, 085122 (2016).
41. Banerjee, K. *et al.* Defect-induced negative magnetoresistance and surface state robustness in the topological insulator BiSbTeSe₂. *Phys. Rev. B* **90**, 235427 (2014).

42. Neupane, M. *et al.* Gigantic Surface Lifetime of an Intrinsic Topological Insulator. *Phys. Rev. Lett.* **115**, 116801 (2015).

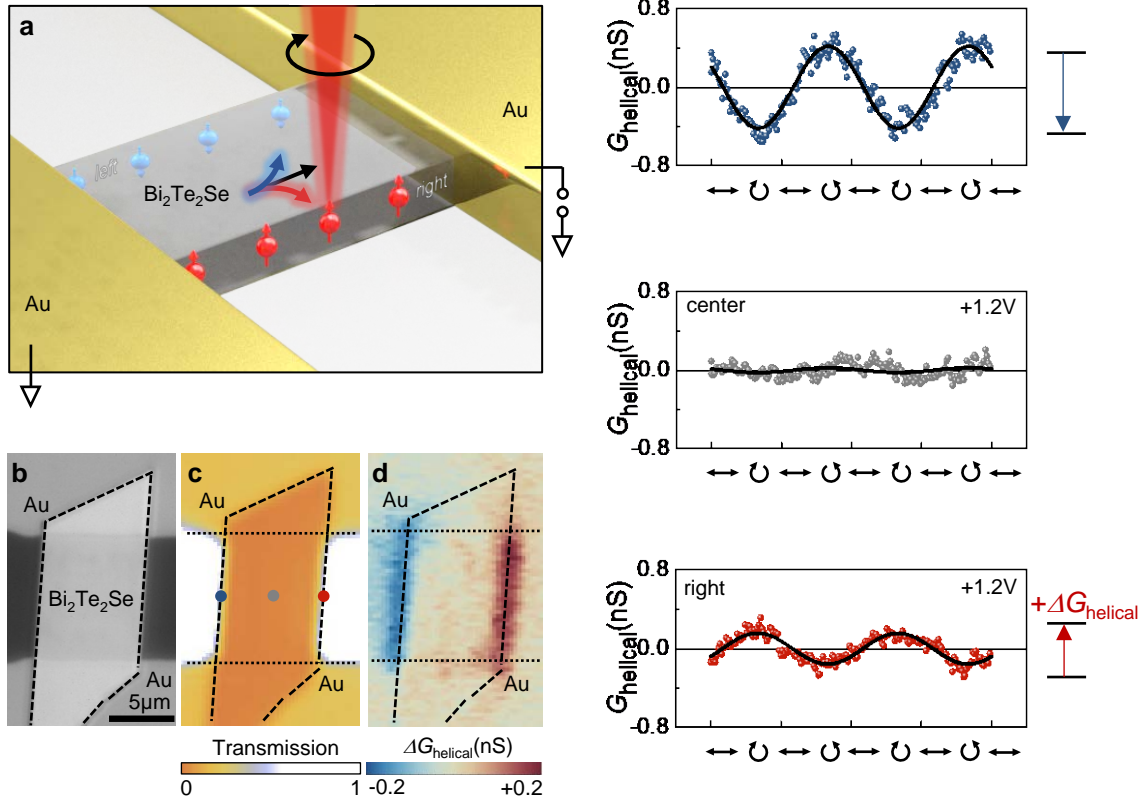


Figure 1 | Helicity-dependent edge conductance at room temperature. **a**, Sketch of a Bi₂Te₂Se (BTS) platelet embedded in a metal/topological-insulator/metal geometry excited by circularly polarized light at perpendicular incidence. Red (blue) spheres represent the electron spin polarization on the right (left) facet of the platelet, when a bias voltage V_{sd} is applied between source to drain. Correspondingly, an electron current density j flows. **b**, Optical microscope image of a BTS platelet (highlighted by dashed lines), contacted by two Ti/Au contacts. **c**, Optical transmission image of the platelet in (b), recorded with laser scanning microscopy. **d**, Simultaneously measured spatial map of the photoconductance generated by the circularly polarized light at a bias voltage $V_{\text{sd}} = 1.2$ V. We use a photo-elastic modulator detecting the difference $\Delta G_{\text{helical}} = G_{\text{helical}}(\sigma^-) - G_{\text{helical}}(\sigma^+)$ of photoconductance which depends on the circularly left (σ^-) and right (σ^+) polarized light. **e-g**, G_{helical} as a function of the laser polarization at the left and right edge, as well as the center [cf. blue, gray, and red dots in (c)]. The polarization is controlled by a quarter waveplate. The symbol ↔ denotes linearly polarized, ↻ circularly right polarized light, ↺ circularly left polarized light. All measurements are performed at $V_{\text{sd}} = +1.2$ V, $P_{\text{laser}} = 230$ μ W, and room temperature.

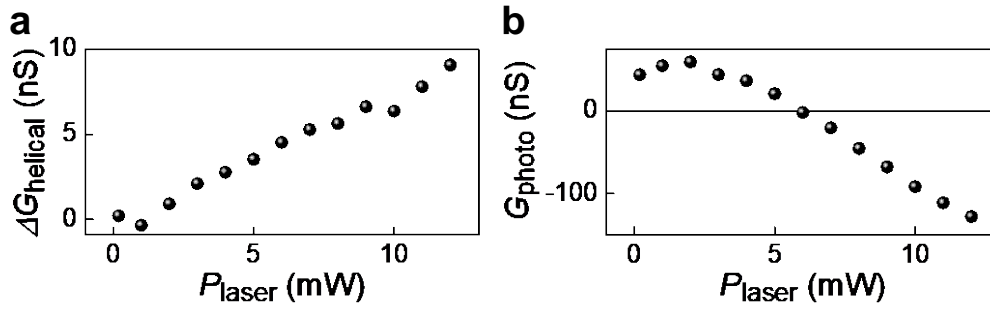


Figure 2 | Irradiance dependence of helical and polarization-independent photoconductance. **a**, The helical $\Delta G_{\text{helical}}$ is linear up to the largest laser powers investigated, and can be tuned to be positive or negative. The polarity depends on the helicity of the exciting photons and the direction of the dark current in the platelets. We show $\Delta G_{\text{helical}}$ for a right edge of a BTS platelet at a positive bias $V_{\text{sd}} = +0.55\text{V}$ (cf. Supplemental Figure S5). **b**, The polarization-independent photoconductance G_{photo} of the BTS platelets shows a non-linear power dependence. The non-linearity is an interplay of saturating photoconductance contributions of the surface and bulk states of the BTS platelet (saturating for $P_{\text{laser}} \geq 5\text{ mW}$) and a negative bolometric photoconductance dominating at large laser powers [cf. ref.12]. All measurements are performed at room temperature.

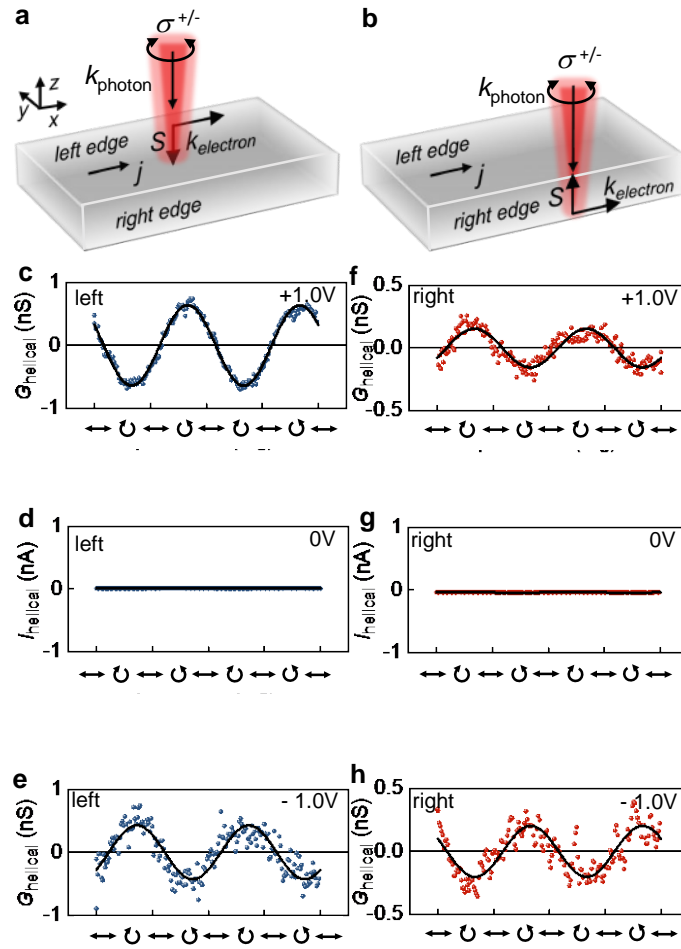


Figure 3 | Helicity, bias, and facet dependence of helical photoconductance. **a, b** Sketch of a BTS platelet with dark current j along the x -direction, when a bias V_{sd} is applied. The current defines the direction of the electron wave vector k_{electron} at the left and right edge. The electron spin-polarization S is perpendicular to k_{electron} and points in opposite directions at the two edges. In (a) [(b)], the left [right] edge is excited with a circularly polarized light with the photon wave vector k_{photon} pointing downwards. **c - e**, $\Delta G_{\text{helical}}$ vs the laser helicity at the left edge for $V_{\text{sd}} = +1$ V (c), 0 V (d), and -1 V (e). The polarization is tuned with a quarter waveplate for an excitation scheme as sketched in (a). **f - h**, Similar data for the right edge for an excitation scheme as sketched in (b). All measurements are performed at $P_{\text{laser}} = 230 \mu\text{W}$ and room temperature.

	G_{helical}	G_{photo}	I_{edge}
$V_{\text{sd}} \rightarrow -V_{\text{sd}}$	-1	-1	0
$\sigma^+ \rightarrow \sigma^-$	-1	+1	-1
$k_{\text{photon}} \rightarrow -k_{\text{photon}}$	+1	+1	+1
<i>left edge</i> \rightarrow <i>right edge</i>	-1	+1	-1

Table 1 | Symmetry chart of G_{helical} , G_{photon} , and edge photocurrent phenomena. Symmetry characteristics of $\Delta G_{\text{helical}}$, G_{photo} , and edge photocurrent effects I_{edge} for changing V_{sd} to $-V_{\text{sd}}$, σ^+ to σ^- , k_{photon} to $-k_{\text{photon}}$, and the excitation position from the left to the right edge of the BTS platelets. A value '-1' states a sign change under the symmetry operation, while '+1' states a sign conservation. The value '0' denotes that I_{edge} is independent from j and the bias.

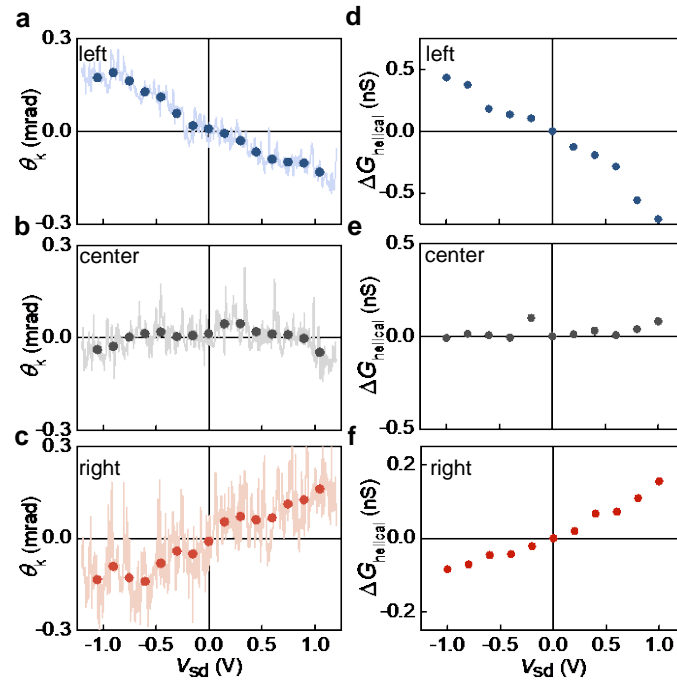


Figure 4 | Kerr angle and helical photoconductance vs bias voltage. **a - c**, Kerr angle θ_K vs the applied bias V_{sd} at the left edge (a), center (b), and right edge (c) of a BTS platelet ($P_{laser} = 400 \mu W$). **d - f**, Corresponding $\Delta G_{helical}$ vs the applied bias V_{sd} ($P_{laser} = 230 \mu W$). All measurements are performed at room temperature.

Spin Hall photoconductance in a 3D topological insulator at room temperature

Paul Seifert¹, Kristina Vaklinova², Sergey Ganichev³, Klaus Kern^{2,4}, Marko Burghard² and Alexander W. Holleitner^{1,*}

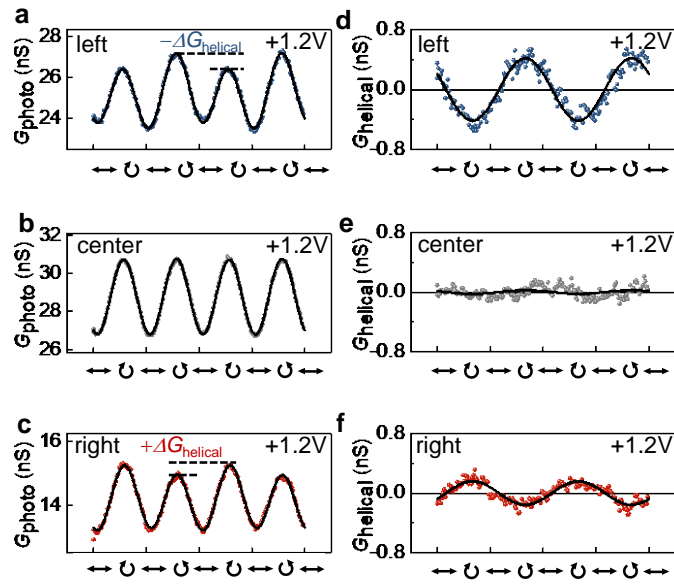
¹Walter Schottky Institut and Physik-Department, Technische Universität München, Am Coulombwall 4a, D-85748 Garching, Germany.

²Max-Planck-Institut für Festkörperforschung, Heisenbergstraße 1, D-70569 Stuttgart, Germany.

³Terahertz Center, University of Regensburg, D-93040 Regensburg, Germany.

⁴Institut de Physique, Ecole Polytechnique Fédérale de Lausanne, CH-1015 Lausanne, Switzerland.

- Supplementary information -



Supplementary Figure S1 | Fitting procedure of the helical photoconductance. **a, b, c,** Original data of the photoconductance vs the polarization of the exciting photons as depicted in Figs. 1e, 1f, and 1g of the main manuscript before subtracting a background which depends on the linear polarization of the photon and a background which is independent of the polarization. The helicity-dependent contribution is indicated by $-\Delta G_{\text{helical}}$ and $+\Delta G_{\text{helical}}$. **d, e, f,** Helical photoconductance G_{helical} which depends on the circularly right (σ^+) and left (σ^-) polarized light of (a)-(c) after subtracting the background.

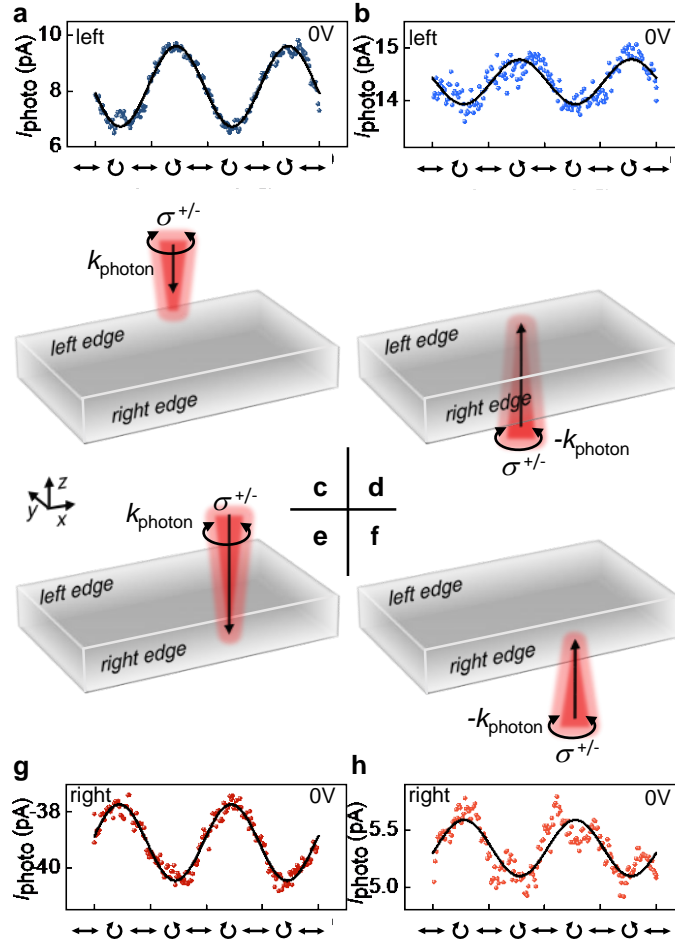
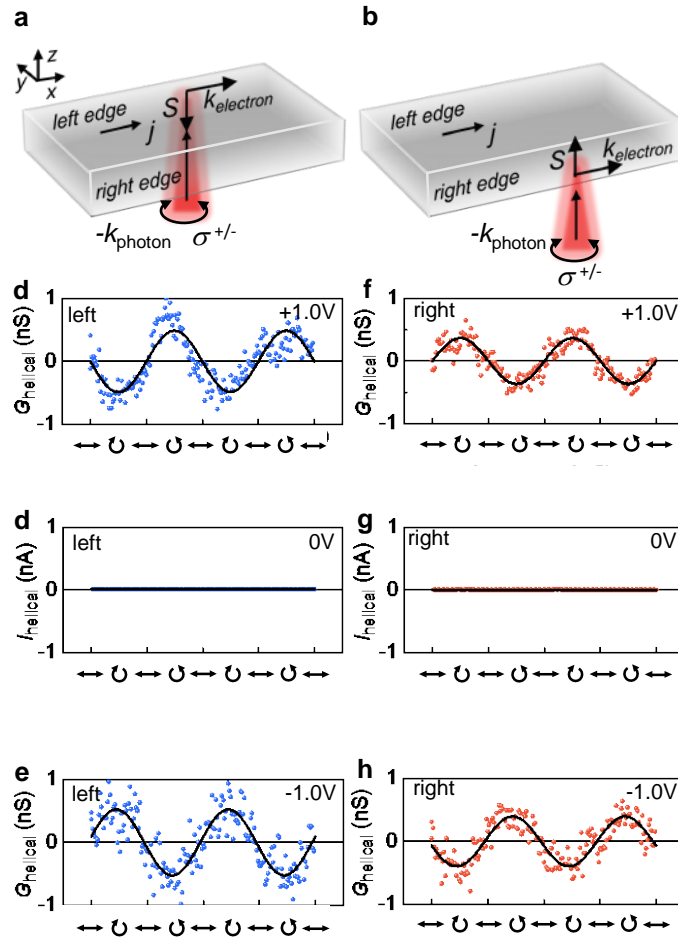


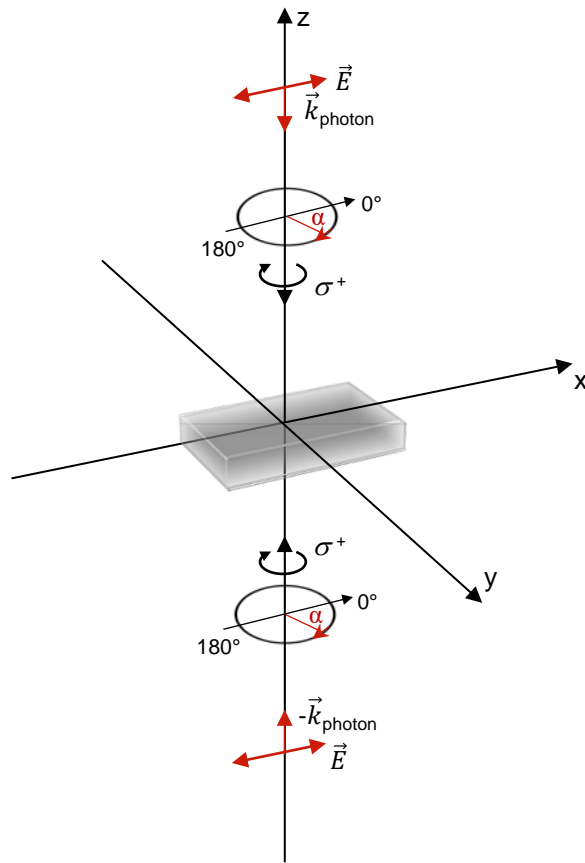
Figure S2 | Helicity dependent edge photocurrents at zero bias. **a**, and **b**, Photocurrent I_{photo} at zero bias ($V_{\text{sd}} = 0$ V) for exciting the left side facet of the platelet as discussed in Figs. 1, 3, and 4 of the main manuscript, for a photoexcitation incident from the top (**a**) and backside (**b**) of the platelet. The polarization is controlled with a quarter waveplate. **c**, and **d**, Schematic illustrations for an excitation at the left side facet with a k_{photon} pointing downwards (**c**) and upwards (**d**). **e**, and **f**, Schematic illustrations for an excitation at the right side facet with a k_{photon} pointing downwards (**e**) and upwards (**f**). **g**, and **h**, I_{photo} at zero bias ($V_{\text{sd}} = 0$ V) for exciting the right side facet of the platelet for a photoexcitation incident from the top (**g**) and from the backside (**h**). The polarization is controlled with a quarter waveplate.

Importantly, we note that for the side facets, the incidence occurs effectively at an oblique angle of $\sim 90^\circ$. Hereby, photocurrents, such as the circular photogalvanic, are possible.³⁵ However, I_{photo} exhibits a rather small amplitude of only pA, which is 1000x smaller than the G_{helical} at $V_{\text{sd}} = 1$ V (cf. Fig. 1). The small signal of I_{photo} is consistent with the optical cross section of the side facets of only $\sim 10^{-2}$ of the overall laser spot of ~ 1.5 μm .

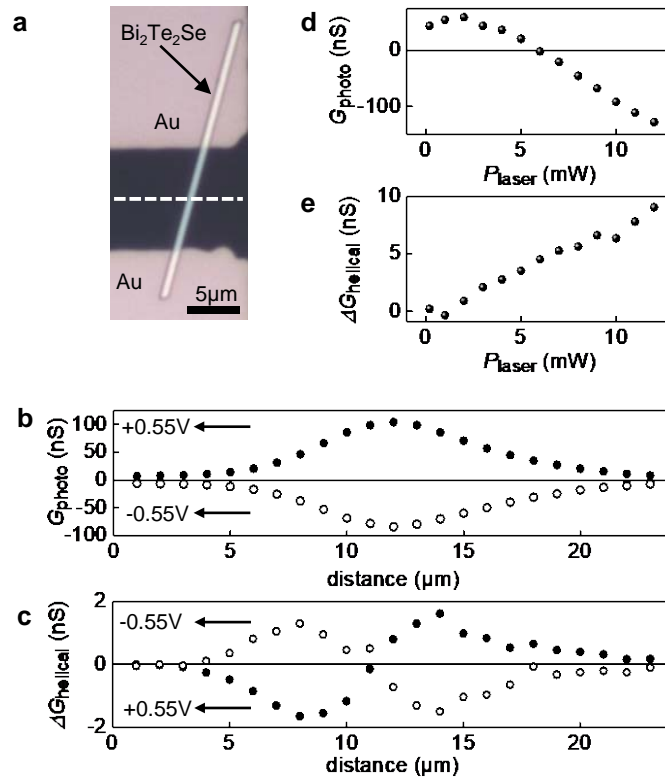


Supplementary Figure S3 | Helical photoconductance at an opposite photon wave vector.

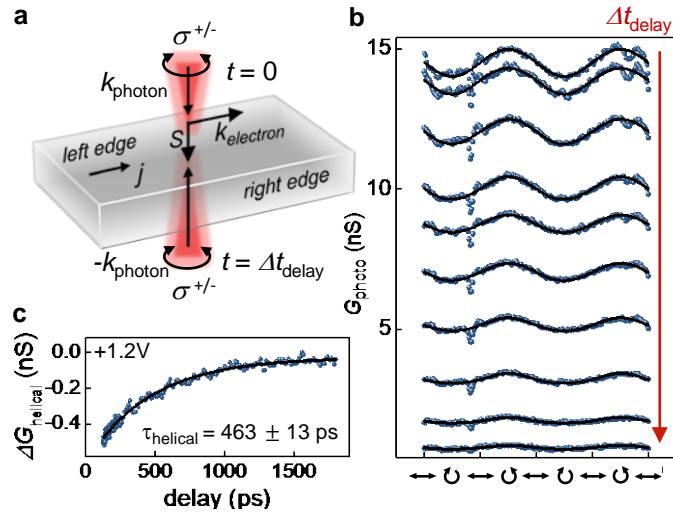
This graph shows supplementary data on the BTS platelet as discussed in Figs. 1, 3, and 4 of the main manuscript, but for a photo-excitation from the backside of the platelet. In other words, the photon wave vector is $-k_{\text{photon}}$ instead of $+k_{\text{photon}}$. **a**, and **b**, Schematic illustrations for the excitation configurations of the measurements in (c),(d),(e) and (f), (g), (h) respectively. **c**, **d**, **e**, Helical photoconductance G_{helical} as a function of the laser polarization at the left edge (as depicted in (a)), for applied bias voltages of $V_{\text{sd}} = +1$ V, $V_{\text{sd}} = 0$ V and $V_{\text{sd}} = -1$ V. **f**, **g**, **h**, Helical photoconductance G_{helical} as a function of the laser polarization at the right edge (as depicted in (b)), for applied bias voltages of $V_{\text{sd}} = +1$ V, $V_{\text{sd}} = 0$ V and $V_{\text{sd}} = -1$ V. We note that for $V_{\text{sd}} = 0$ (Supplementary Figs. S3d and S3g), we plot the originally detected signal $I_{\text{helical}} \sim 0$ nA instead of G_{helical} , because a photoconductance cannot be defined at zero bias. The polarization is controlled with a quarter waveplate.



Supplementary Figure S4 | Polarization and sample configuration. Sketch of the measurement geometry and polarization optics circuitry. The quarter waveplates are arranged in a way, that the sense of rotation of the incoming laser light is defined globally and not with respect to the surface normal of the sample.



Supplementary Figure S5 | Helical photoconductance in a narrow BTS platelet. **a**, Optical microscope image of a narrow BTS nanoplatelet with a length of $\sim 27 \mu\text{m}$, a width of $\sim 300 \text{ nm}$, and a height of 95 nm contacted by two Ti/Au contacts with a distance of $10 \mu\text{m}$. This is sample of the data as discussed in Fig. 2 of the main manuscript. **b**, Total photoconductance G_{photo} vs position along the white dashed line in (a) for $V_{\text{sd}} = +0.55 \text{ V}$ (full circles) and -0.55 V (open circles). The measurements are performed at room temperature and $P_{\text{laser}} = 1.7 \text{ mW}$. **c**, Corresponding $\Delta G_{\text{helical}}$ along the white dashed line in (a). **d**, Photoconductance G_{photo} as a function of incident laser power at $V_{\text{sd}} = +0.55 \text{ V}$. Same graph as Fig. 2b. **e**, Corresponding $\Delta G_{\text{helical}}$ as a function of incident laser power at $V_{\text{sd}} = +0.55 \text{ V}$. Same graph as Fig. 2a.



Supplementary Figure S6 | Decay time of the helical photoconductance. **a**, Schematic illustrations for measuring the auto-correlation of the helical photoconductance, when a finite bias V_{sd} is applied, and correspondingly, an electron current density j flows. **b**, Time-resolved pump/probe auto-correlation measurements at the left edge of a BTS platelet as a function of laser polarization. The top curve is recorded at a time-delay $\Delta t_{\text{delay}} = 0$ ps between the pump and probe pulse. The bottom curve is recorded at $\Delta t_{\text{delay}} = 1800$ ps. **c**, $\Delta G_{\text{helical}}$ as function of the time-delay Δt_{delay} between pump- and probe-pulse. Measurement parameters are $P_{\text{pump}} = 1$ mW, $P_{\text{probe}} = 2$ mW, $V_{sd} = +1.2$ V. The dimensions of the investigated BTS platelet are: length ~ 20 μm , width = 8.9 μm , height = 90 nm.